Industrial Crops & Products 249 (2026) 123746

Contents lists available at ScienceDirect

Industrial Crops & Products

journal homepage: www.elsevier.com/locate/indcrop

Resonance frequency-based mechanical grading of fast-grown Chinese fir: Assessing the contribution of vision-based knot detection

Fanxu Kong [a], Shuke Jia [a], Feibin Wang [b], Tianjun Xie [a], Jinqiu Xie [a], Zeli Que [a,*], Jianzhang Li [c]

[a] *Co-Innovation Center of Efficient Processing and Utilization of Forest Resources, College of Material Science and Engineering, Nanjing Forestry University, Nanjing, Jiangsu 210037, China*
[b] *College of Landscape Architecture, Nanjing Forestry University, Nanjing, Jiangsu 210037, China*
[c] *State Key Laboratory of Efficient Production of Forest Resources, Beijing Forestry University, Beijing 100083, China*

ARTICLE INFO

Keywords:
Fast-grown Chinese fir
Resonance frequency method
Knot detection
Mechanical grading

ABSTRACT

Chinese fir (*Cunninghamia lanceolata* (Lamb.) Hook), a fast-grown plantation species widely available in China, remains underutilized in structural applications due to the absence of standardized grading systems. This study evaluated the effectiveness of a resonance frequency-based grading approach for structural Chinese fir, assessed the supplementary contribution of vision-based knot detection, and examined the main factors governing strength class assignment under the EN 338 framework. Dynamic modulus of elasticity (MOE) derived from the resonance frequency method, density, and static bending properties were determined for 102 specimens. Knot-related indicators, including the knot diameter ratio (KDR) and concentrated knot diameter ratio (CKDR), were quantified from surface images using a vision-based method in accordance with JAS 1083. The results showed that incorporating predicted maximum wide-face CKDR together with dynamic MOE improved the prediction of bending MOE ($R^2 = 0.64$) and bending strength ($R^2 = 0.46$) compared with dynamic MOE alone, and that local and global density showed a clear correlation ($R^2 = 0.67$). Grading results showed that 19.6% (20), 45.1% (46), and 35.3% (36) were classified as C20, C14, and Reject, respectively, and that density was the most critical grade determining property (GDP) limiting assignment to higher strength classes. These results support the effectiveness of dynamic MOE as the primary indicating property relevant to Chinese fir grading, while automated knot detection provided supplementary information with limited influence on final grade yield under EN 338. Overall, this study provides a preliminary standard-linked basis for deriving and verifying EN 338 grading settings for fast-grown Chinese fir using resonance-based dynamic MOE alone and in combination with vision-based knot indicators. Future studies should examine broader Chinese fir populations and reassess the grading value of more refined knot-related indicators.

1. Introduction

In China, load-bearing materials used in modern timber buildings rely heavily on imported timber products, despite the country possessing the world's largest area of planted forests (Wang et al., 2023, 2025b). Chinese fir (*Cunninghamia lanceolata* (Lamb.) Hook) is one of the most widely planted plantation species. However, its broader application in modern structural sawn timber and engineered wood products remains constrained by the limited availability of practical standard-linked grading approaches (Gong et al., 2024; Kong et al., 2025). This limitation also reflects a broader challenge for the high-value structural utilization of domestic plantation timber resources.

Mechanical grading provides an effective means for grading structural timber with objective indicating properties (IPs) obtained from non-destructive measurements (Ridley-Ellis et al., 2016, 2022). Previous studies have shown that resonance frequency-based dynamic modulus of elasticity (MOE) can provide grading reliability comparable to machine stress rating (MSR), while remaining relatively simple, economical, and compatible with optical or vision-based inspection systems (Oscarsson et al., 2014; Olsson and Oscarsson, 2017; Abdeljaber et al., 2023). Good relationships between dynamic MOE and bending properties have been reported for plantation species such as radiata pine (*Pinus radiata* D. Don) (Arriaga et al., 2014), southern pines (*Pinus* spp.) (Uzcategui et al., 2023), and eucalyptus (*Eucalyptus nitens*) (Ettelaei et al., 2022). These

* Corresponding author.
E-mail address: zelique@njfu.edu.cn (Z. Que).

https://doi.org/10.1016/j.indcrop.2026.123746
Received 1 April 2026; Received in revised form 20 May 2026; Accepted 18 June 2026

findings provide a sound basis for extending resonance frequency-based grading approaches to fast-grown Chinese fir.

For Chinese fir, several studies have explored grading strategies through the definition of custom dynamic MOE intervals, and have shown that appropriate layup configurations can effectively improve the mechanical performance of glued laminated timber and cross-laminated timber (Huang et al., 2023; Gong et al., 2024; Yin et al., 2024). Subsequent research based on the JAS 1152 (Ministry of Agriculture, Forestry and Fisheries, 2023) verified the applicability of resonance-based testing for Chinese fir lamellas and established dynamic MOE grading thresholds (Kong et al., 2025). However, its alignment with the EN 338 (European Committee for Standardization, 2016a) strength class system remains unclear. Similar limitations also affect direct application to Chinese standards for structural sawn timber (GB/T 36407 (Standardization Administration of China, 2018)) and cross-laminated timber (LY/T 3039 (National Forestry and Grassland Administration, 2018)).

Although dynamic MOE is an effective predictor, additional defect-related information may further improve the prediction of mechanical properties. Among visible features, knots are particularly important because they are associated with fiber deviation, local cross-sectional reduction, and stress concentration (Collins and Fink, 2022; Wang et al., 2025a). Previous studies have shown that knot-related indicators can provide additional information for estimating bending properties in several species (Wright et al., 2019; França et al., 2020; Barriola et al., 2021). Therefore, for Chinese fir grading, knot-related indicators are more appropriately viewed as potential supplements to resonance-based dynamic MOE, and their practical contribution to improving prediction accuracy still needs to be clarified.

A practical challenge is how to obtain such knot-related information in a manner that is objective, efficient, and compatible with industrial grading workflows. Grading standards in different regions adopt markedly different definitions and quantification rules for knot (British Standards Institution, 2007; Ministry of Agriculture, Forestry and Fisheries, 2019; National Lumber Grades Authority, 2022). In this regard, JAS 1083 (Ministry of Agriculture, Forestry and Fisheries, 2019) provides a useful framework because it defines the knot diameter ratio (KDR) and concentrated knot diameter ratio (CKDR) directly from surface measurements without requiring reconstruction of the projected knot area on the cross-section. This makes automated surface-based detection a more practical route for deriving grading-relevant knot indicators. In recent years, computer vision and deep learning have enabled extensive research on automated wood defect detection from surface images (Gao et al., 2021; An et al., 2024; Ji et al., 2024; Jambreković et al., 2024; Kılıç et al., 2025; Shi et al., 2025). However, comparatively less attention has been paid to transforming detected knot information into grading-relevant indicators that are compatible with structural grading standards.

Against this background, this study tested the hypothesis that knot-related indicators derived from surface images could provide supplementary information beyond resonance frequency-based dynamic MOE for predicting bending properties and grading outcomes. The relationships among dynamic MOE, vision-based knot indicators quantified according to JAS 1083 (Ministry of Agriculture, Forestry and Fisheries, 2019), and the grade determining properties (GDPs) defined in EN 338 (European Committee for Standardization, 2016a) were analyzed. On this basis, univariate and multivariate regression-based grading models were established, and their grading performance was evaluated through the procedures specified in EN 14081–2 (European Committee for Standardization, 2018). The main contribution of this study lies in integrating resonance-based dynamic MOE with vision-based knot indicators within an EN 338 (European Committee for Standardization, 2016a) / EN 14081–2 (European Committee for Standardization, 2018) grading workflow, thereby clarifying their respective roles in the mechanical grading of fast-grown Chinese fir. Rather than claiming a fully optimized industrial grading system, this study aimed primarily to verify the effectiveness of resonance-based grading for Chinese fir under the EN 338 (European Committee for Standardization, 2016a) framework, while also evaluating the supplementary role of vision-based knot indicators within this grading workflow.

2. Material and methods

2.1. Material and specimens

Timber from Chinese fir trees from Nanping, Fujian Province, China, was used in this study. The trees were 10–13 years old. A total of 260 sawn timber specimens with nominal dimensions of 3000 × 90 × 35 mm were prepared. Prior to testing, all specimens were stacked with spacers and conditioned at room temperature for approximately three months to achieve moisture equilibrium. Standard moisture content corrections were then applied to the measured density and mechanical properties. Summary statistics of moisture content, density, and mechanical properties are presented in Table 5 (**Section 3.4**).

All 260 specimens were measured for dimensions, imaged on all four longitudinal surfaces, and tested for longitudinal dynamic MOE. Among them, 106 specimens were reserved for the test subset of the knot detection dataset, and 102 of these were subsequently subjected to destructive bending tests. After bending, local density and moisture content were measured for the same specimens. Dimensions were measured in accordance with EN 1309–1 (European Committee for Standardization, 1997), while the detailed procedures for image acquisition, knot-indicator quantification, density measurement, and mechanical testing are described in **Sections 2.2–2.4**.

2.2. Timber and knot dataset construction

2.2.1. Image acquisition

Surface images were acquired from the Chinese fir specimens to support timber and knot detection. Images were taken from both wide faces (F1, F2) and narrow edges (E1, E2) of each specimen using a Canon EOS 50D camera at a resolution of 4752 × 3168 pixels. Each specimen was divided along its length into five equal segments (S1–S5), each 600 mm long, and one image was captured for each segment on each surface. In addition, one scale-reference image was taken for the wide face and one for the narrow face. Thus, 22 original images were obtained for each specimen. The pixel-to-millimeter conversion factor was determined using ImageJ (Schneider et al., 2012). A schematic illustration of the image acquisition procedure is shown in Fig. 1.

2.2.2. Image preprocessing and annotation

To reduce background interference, the acquired images were cropped in the height direction while preserving the timber contour, leaving minimal background around the specimen edges (Fig. 2).

The cropped images were then annotated using VoTT software (Microsoft, 2021) with two object classes, namely knots and timber surfaces. In the present study, knot annotation and quantification did not distinguish between knot types, and all visible knots were treated as a single defect category for indicator calculation.

To emulate real production conditions where timber is continuously conveyed and images are acquired in real time, the annotated images were further cropped and rotated. Using images with scale references, 150 mm was converted to pixels, and cropping and rotation were performed using the *AtLeastOneBBoxRandomCrop* function in the *Albumentations* package (Buslaev et al., 2020). This process guaranteed the inclusion of at least one annotated object and automatically adjusted the bounding boxes and was randomly repeated three times for augmentation (Fig. 3). This augmentation strategy generated local image patches while preserving valid timber and knot annotations, and introduced variation in the relative position and orientation of annotated objects within the cropped images. In this way, the cropping operation was used to simulate local field-of-view changes that may occur in future

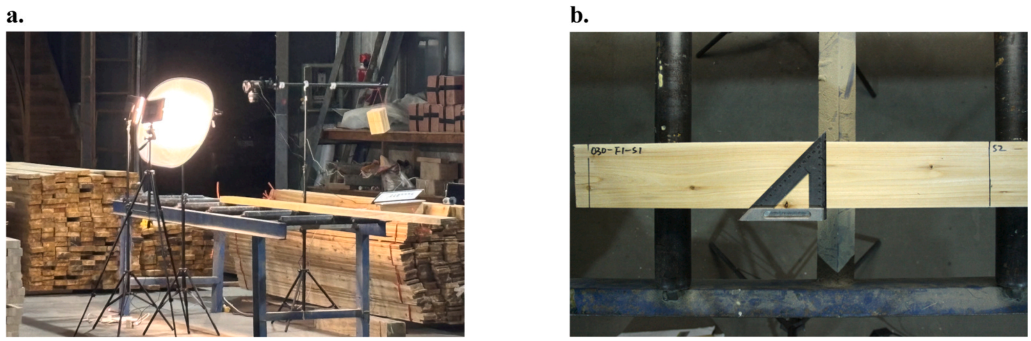

Fig. 1. Surface image acquisition of timber specimens: (a) image capture of specimen surfaces; (b) specimen image with scale reference.

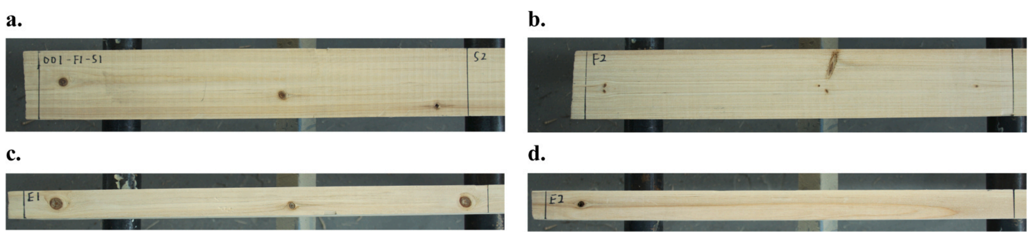

Fig. 2. Images cropped along the height direction: (a) F1; (b) F2; (c) E1; and (d) E2.

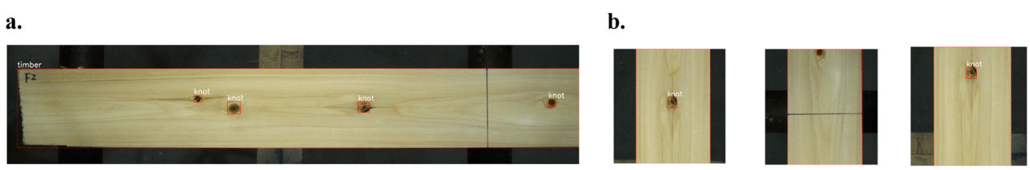

Fig. 3. Image pre-processing using *Albumentations* (Buslaev et al., 2020): (a) original annotated image and (b) cropped and rotated annotated images.

continuous image acquisition scenarios, thereby improving the detector's robustness to specimen placement and object-position variation. Because the augmented images were produced from the same material source and imaging setup, this strategy should be interpreted mainly as improving robustness to geometric variation rather than as a full validation of generalization across different acquisition conditions.

2.2.3. Dataset composition and split

The final dataset comprised 15600 images, including 7392 training images, 1848 validation images, and 6360 test images, as summarized in Table 1. This dataset design ensured that model evaluation was conducted on specimens that were fully separated from those used for training and validation, thereby avoiding specimen-level data leakage during model development.

Table 1
Dataset division for Chinese fir knot detection, including training, validation, and test sets.

Dataset	Number of specimens	Number of images	Percentage (%)
Training	154	7392	47.38
Validation		1848	11.85
Test	106	6360	40.77
Total	260	15600	100.00

Note: The training and validation images were derived from the same pool of 154 specimens, whereas the test images were obtained from a separate set of 106 specimens.

2.3. Detection model and calculation of knot-related indicators

2.3.1. Model training and selection

All models were trained and evaluated on a workstation running Windows 11 and equipped with an NVIDIA GeForce RTX 4060 GPU (8 GB VRAM). To compare detection accuracy and computational efficiency, representative lightweight and medium-scale YOLO models from versions 3–12 were evaluated and built upon the Ultralytics library (Ultralytics, 2025). All models were initialized with pretrained weights and trained under the same settings: 100 epochs, batch size 16, input image size 640, automatic optimizer selection, initial learning rate 0.01, momentum 0.937, weight decay 0.0005, and early stopping with a patience of 30 epochs. Model performance was assessed using precision, recall, F1-score, AP@50, AP@50:95, and inference speed.

The selected model was then used to detect knots and timber regions in the surface images and to derive knot-related indicators for later analyses.

2.3.2. Calculation of knot-related indicators

Knot-related indicators were calculated in accordance with JAS 1083 (Ministry of Agriculture, Forestry and Fisheries, 2019). Two surface-based indicators were considered: the knot diameter ratio (KDR) and the concentrated knot diameter ratio (CKDR). KDR is defined as the ratio of the diameter of an individual knot to the width of the timber surface on which the knot appears. CKDR is defined as the sum of knot diameter ratios within a specified evaluation length of 150 mm along the timber.

The indicators were calculated using Eq. (1) and Eq. (2):

$$\mathrm{KDR} = \frac{d_i}{b} \tag{1}$$

$$\mathrm{CKDR} = \sum_{i=1}^{n} \frac{d_i}{b} \tag{2}$$

where d_i is the diameter of the i-th knot (mm), b is the surface width of the timber at the knot location (mm), n is the number of knots within the 150 mm evaluation length.

The dataset for knot size prediction consisted of images from five longitudinal segments (S1–S5) of each specimen in the bending-test population. Pixel-to-millimeter conversion factors for the wide and narrow surfaces were determined using ImageJ (Schneider et al., 2012), and the pixel length corresponding to 150 mm was obtained.

For each segment, a 150 mm prediction window was slid along the longitudinal direction, and knot and timber objects within each window were detected using the selected YOLO model (Fig. 4). The 5 mm step size was adopted as a practical setting for automated evaluation. Because the prediction window used for knot-indicator calculation was 150 mm, this step corresponded to only 1/30 of the window length and resulted in highly overlapping adjacent windows. Since the maximum KDR and CKDR were determined from all sliding windows rather than from a single fixed window position, this setting was considered sufficiently fine to reduce boundary-related effects while maintaining computational efficiency. Based on the predicted bounding boxes, the KDR and CKDR were calculated, where the width of the timber bounding box represented the timber surface width and the width of the knot bounding box represented the knot diameter. The maximum KDR and CKDR over all sliding windows were then determined for the wide and narrow surfaces of each specimen across all five segments.

The same procedure was applied to manually labeled bounding boxes from the original images to obtain reference values to evaluate the accuracy of knot detection and knot indicator calculation.

In addition to considering each wide-face or narrow-face knot indicator individually, a composite knot indicator was also defined following JAS 1083 (Ministry of Agriculture, Forestry and Fisheries, 2019) for structural timber of Class I, Type A. Under this classification, only wide-face KDR and CKDR are used for grading in this study, and the corresponding three-level criteria are listed in Table 2.

For each wide-face knot indicator, a continuous grade-related value was calculated using linear interpolation following Moriguchi et al. (Moriguchi et al., 2016) using Eq. (3). A composite knot indicator (k_G) was then defined as the maximum of the two interpolated wide-face indicators using Eq. (4):

$$g_t(k_t) = \begin{cases} n - 1 + \dfrac{k_t - l_{t,n-1}}{l_{t,n} - l_{t,n-1}}, & l_{t,n-1} < k_t \le l_{t,n}, n = 1,2,3 \\[2ex] 3 + \dfrac{k_t - l_{t-3}}{l_{t,3} - l_{t,2}}, & k_t > l_{t,3} \end{cases} \tag{3}$$

$$k_G = \max\{g_t(k_t) \mid t \in \{\mathrm{KDR},\ \mathrm{CKDR\ (face)}\}\} \tag{4}$$

where k_t is the quantified knot indicator type (KDR or CKDR), $l_{t,n}$ denotes the threshold for each grade interval ($n = 1, 2, 3$).

Following this procedure, both individual and composite knot-related indicators were obtained. The symbols and definitions of all

Table 2
Knot criteria for structural timber surfaces in JAS 1083 (Ministry of Agriculture, Forestry and Fisheries, 2019) (Type A, Class I).

Knot indicator type	Grade		
	1	2	3
KDR	0.2	0.4	0.6
CKDR	0.3	0.6	0.9

Note: According to JAS 1083 (Ministry of Agriculture, Forestry and Fisheries, 2019), structural timber is classified as Class I, Type A when the short side of the end section is less than 36 mm, or when the short side is 36 mm or greater and the long side is less than 90 mm. The specimens used in this study had a nominal thickness of 35 mm and therefore fell within this classification.

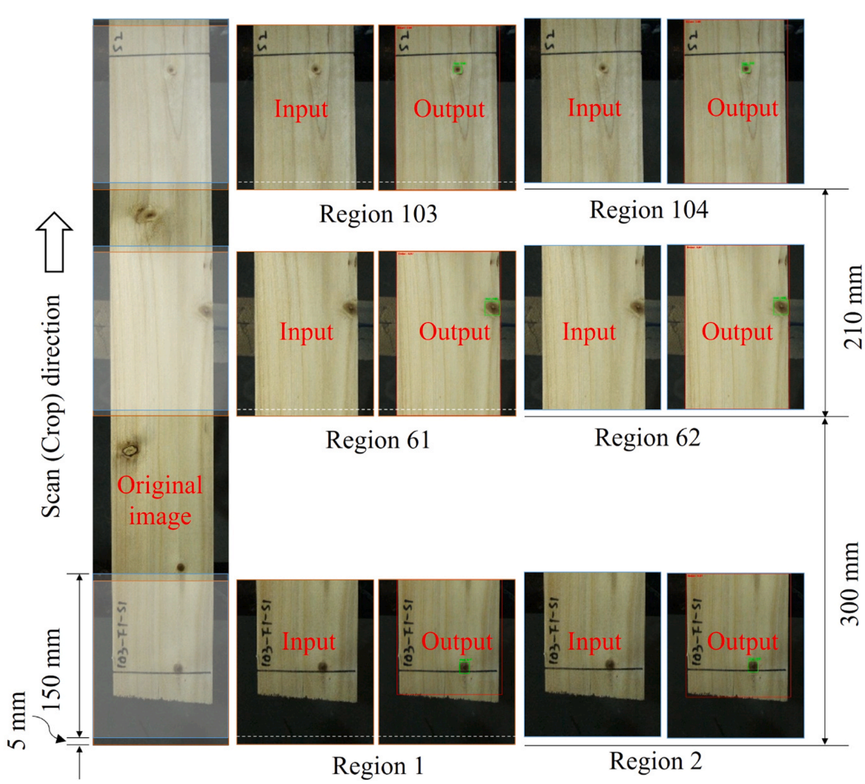

Fig. 4. Schematic illustration of knot prediction using a sliding-window approach.

indicators used in this study are summarized in Table 3.

2.4. Physical and mechanical properties

2.4.1. Density and moisture content measurements

During the non-destructive testing stage, the global density (ρ_{global}) was calculated based on the overall mass and volume of each specimen.

After the bending tests, moisture content (u) and local density (ρ_{local}) were determined for the destructively tested specimens. For this purpose, a 20 mm long full cross-sectional sample was cut as close as possible to the failure location of each specimen. In accordance with EN 408 (European Committee for Standardization, 2012), the sample section was selected to be free from knots and resin pockets. Moisture content was measured using the oven-dry method, and local density was calculated from the measured mass and volume of the sample.

Following EN 384 (European Committee for Standardization, 2016b) and reference (Olsson and Oscarsson, 2017), both local and global densities were adjusted to a reference moisture content of 12% using Eq. (5) and Eq. (6). Here, u_s represents the mean moisture content of all the specimens.

$$\rho_{\text{local,corr}} = \rho_{\text{local}}(1 - 0.005(u - 12)) \tag{5}$$

$$\rho_{\text{global,corr}} = \rho_{\text{global}}(1 - 0.005(u_s - 12)) \tag{6}$$

2.4.2. Dynamic MOE tests

Dynamic MOE was determined using the resonance frequency method (Kong et al., 2025). During testing, each specimen was simply supported, excited by an impulse at one end, and the vibration response was recorded at the opposite end. The first longitudinal resonance frequency (f) was extracted in the frequency domain and used to calculate dynamic MOE.

All dynamic MOE values were corrected to a reference moisture content of 12% and are denoted as $E_{\text{dyn,corr}}$ (GPa). The corrected dynamic MOE was calculated using Eq. (7):

$$E_{\text{dyn,corr}} = 4\frac{m}{L \bullet h \bullet b} \bullet f^2 \bullet L^2 \left(1 + \frac{u_s - 12}{100}\right) \times 10^{-9} \tag{7}$$

where f is the first longitudinal frequency (Hz), m is the mass of the specimen (kg), L, h and b are the specimen's length, cross-sectional width, and depth (m), respectively.

2.4.3. Determination of global MOE in bending and bending strength parallel to grain

Bending tests were conducted using a universal testing machine (UTM5105, maximum capacity 100 kN; Shenzhen Sansi Zongheng Technology Co., Ltd., China) in accordance with EN 408 (European Committee for Standardization, 2012) (Fig. 5). Before testing, the critical section of each specimen was identified based on the previously calculated KDR and CKDR values and positioned within the constant-moment region between the two loading points. In accordance with EN 384 (European Committee for Standardization, 2016b), the tension edge was then selected at random after the critical section had been determined.

The loading rate was set to 0.25 mm/s, and each test was terminated when visible damage occurred or when the applied load decreased to less than 80% of the maximum recorded load.

The elastic range was defined as 10%–40% of the maximum failure load, and the global MOE in bending ($E_{\text{m,g}}$) was calculated from the load–deflection data within this range and corrected to a reference moisture content of 12% using Eq. (8):

$$E_{\text{m,g,corr}} = \frac{3al^2 - 4a^3}{2bh^3\left(\frac{\Delta w}{\Delta F} - \frac{6a}{5Gbh}\right)}(1 + 0.01(u - 12)) \bullet 10^{-3} \tag{8}$$

where $E_{\text{m,g,corr}}$ is the global MOE in bending corrected to a reference moisture content of 12% (GPa), a is the distance between a loading point and the nearest support (mm), l is the test span (mm), $\Delta w/\Delta F$ is the increment of deflection per unit load within the elastic range (mm/N), and G is the shear modulus (MPa). Following EN 384 (European Committee for Standardization, 2016b), G was assumed to be infinite. The remaining symbols have the same meanings as defined previously.

The bending strength parallel to grain (f_{m}) was calculated using Eq. (9).

$$f_{\text{m}} = \frac{3F_{\max}a}{bh^2} \tag{9}$$

where $F_{\max}$ is the maximum failure load (N). According to EN 384 (European Committee for Standardization, 2016b), no moisture content correction was applied to f_{m}. However, when the specimen depth was less than 150 mm and the characteristic density did not exceed 700 kg/m^3, a depth correction factor (k_h) was applied. The corrected bending strength ($f_{\text{m,corr}}$) was calculated as Eq. (10) and Eq. (11):

$$f_{\text{m,corr}} = f_{\text{m}}/k_h \tag{10}$$

$$k_h = \min\begin{cases}\left(\frac{150}{h}\right)^{0.2} \\ 1.3\end{cases} \tag{11}$$

2.5. Mechanical grading models and parameter derivation

2.5.1. Calculation of GDPs

2.5.1.1. Bending MOE. According to EN 384 (European Committee for Standardization, 2016b), when the characteristic bending MOE is determined from global MOE tests, $E_{\text{m,g,corr}}$ was first converted to the parallel bending MOE (E_0) using Eq. (12):

$$E_0 = E_{\text{m,g,corr}} \times 10^3 \times 1.3 - 2690 \tag{12}$$

The characteristic mean parallel bending MOE required for each grade, $E_{0,\text{mean}}$, was then calculated using Eq. (13):

$$E_{0,\text{mean}} = \overline{E_0}/0.95 \tag{13}$$

where $\overline{E_0}$ is the arithmetic mean of the sample E_0 values.

2.5.1.2. Bending strength. The characteristic bending strength for each grade, f_{k} was calculated following EN 384 (European Committee for Standardization, 2016b) as Eq. (14):

$$f_{\text{k}} = f_{05} \cdot k_{\text{v}} \tag{14}$$

where f_{05} is the 5th percentile value at 75% confidence level calculated according to EN 14358 (European Committee for Standardization, 2016c), and k_{v} is a variation factor defined in EN 384 (European Committee for Standardization, 2016b). The value of k_{v} was assigned using Eq. (15):

Table 3
Summary of knot-related indicators and symbols.

Knot indicator	Symbol
Maximum KDR of predicted or labeled knots (edges)	$k_{\text{KDR,edge,p(l)}}$
Maximum CKDR of predicted or labeled knots (edges)	$k_{\text{CKDR,edge,p(l)}}$
Maximum KDR of predicted or labeled knots (faces)	$k_{\text{KDR,face,p(l)}}$
Maximum CKDR of predicted or labeled knots (faces)	$k_{\text{CKDR,face,p(l)}}$
Maximum grade-related values from KDR and CKDR interpolation of predicted or labeled knots (faces)	$k_{\text{G,p(l)}}$

Note: Subscripts p and l denote predicted and labeled values, respectively. In total, 10 knot-related indicators are analyzed in this study.

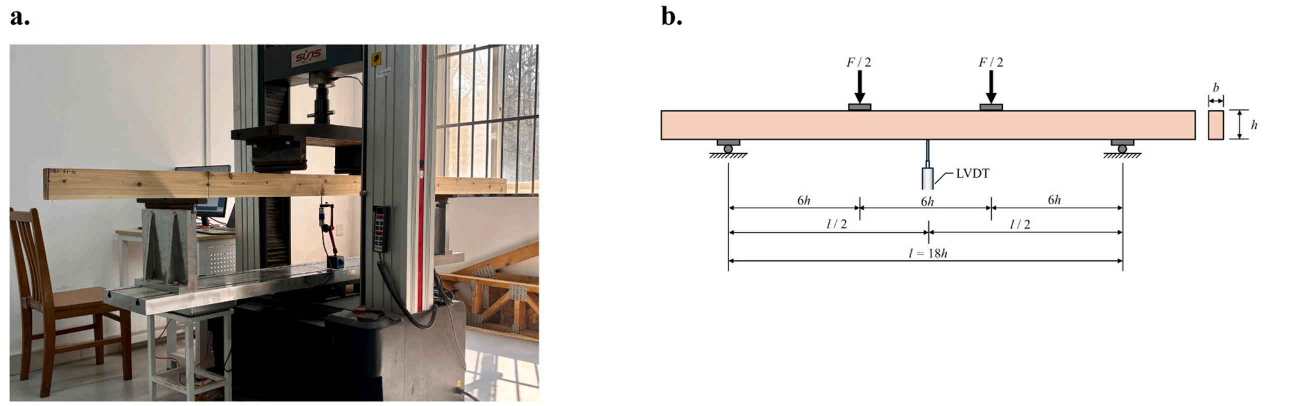

Fig. 5. Setup and schematic diagrams of the edgewise bending tests.

$$k_v = \begin{cases} 1.0, & f_{m,k} < 30 \text{ MPa} \\ 1.12, & f_{m,k} \geq 30 \text{ MPa} \end{cases} \tag{15}$$

where $f_{m,k}$ denotes the target characteristic bending strength of the grade specified in EN 338 (European Committee for Standardization, 2016a).

2.5.1.3. Density. The characteristic density for each grade was defined as the 5th percentile of the local density calculated according to EN 14358 (European Committee for Standardization, 2016c).

2.5.2. Regression models based on IPs

Two types of regression models were established for predicting bending MOE and bending strength from the IPs:

1. univariate regression models based on dynamic MOE and
2. multivariate regression models based on dynamic MOE combined with one selected knot-related indicator.

For the univariate models, $E_{dyn,corr}$ was used as the IP. The predicted characteristic mean parallel bending MOE ($\widehat{E}_{0,mean}$) was calculated as Eq. (16):

$$\widehat{E}_{0,mean} = \frac{\left(a_{E_{m,g,corr}} \cdot \mathrm{IP} + b_{E_{m,g,corr}}\right) \times 10^3 \times 1.3 - 2690}{0.95} \tag{16}$$

where $a_{E_{m,g,corr}}$ and $b_{E_{m,g,corr}}$ are the regression coefficients between $E_{m,g,corr}$ and $E_{dyn,corr}$.

For bending strength, the predicted characteristic value ($\widehat{f}_k$) was calculated using Eq. (17):

$$\widehat{f}_k = \left(a_{f_{m,corr}} \cdot \mathrm{IP} + b_{f_{m,corr}} - t \cdot s_{\delta, f_{m,corr}}\right) k_v \tag{17}$$

where $a_{f_{m,corr}}$ and $b_{f_{m,corr}}$ are the regression coefficients between $f_{m,corr}$ and $E_{dyn,corr}$, $s_{\delta, f_{m,corr}}$ is the standard error of the estimate, and t was taken as 1.645 from the t-distribution with assumed large samples for the 5% prediction level according to EN 14081–2 (European Committee for Standardization, 2018).

For the multivariate models, $\widehat{E}_{m,g,corr}$ and $\widehat{f}_{m,corr}$, predicted from regression models including dynamic MOE and one selected knot-related indicator listed in Table 3, were used as the IPs for grading. The predicted characteristic mean parallel bending MOE was calculated Eq. (18),

$$\widehat{E}_{0,mean} = \frac{\mathrm{IP} \times 10^3 \times 1.3 - 2690}{0.95} \tag{18}$$

and the corresponding characteristic bending strength was calculated using Eq. (19),

$$\widehat{f}_k = \left(\mathrm{IP} - t \cdot s_{\delta, f_{m,corr}}\right) k_v \tag{19}$$

For both univariate and multivariate grading models, density was always predicted from the relationship between global density and local density (IP = $\rho_{global,corr}$). The predicted characteristic density was calculated using Eq. (20):

$$\widehat{\rho}_k = a_{\rho_{local,corr}} \cdot \mathrm{IP} + b_{\rho_{local,corr}} - t \cdot s_{\delta, \rho_{local,corr}} \tag{20}$$

where $a_{\rho_{local,corr}}$ and $b_{\rho_{local,corr}}$ are the regression coefficients between $\rho_{local,corr}$ and $\rho_{global,corr}$, and $s_{\delta, \rho_{local,corr}}$ is the standard error of the estimate.

2.5.3. Calculation of grading settings

Based on the predictive relationships established between the IPs and the GDPs, the grading settings for the univariate regression models were derived as Eq. (21) to Eq. (23):

$$S_{MOE} = \frac{\left(E_{req,0,mean} \cdot 0.95 + 2690\right) / \left(10^3 \times 1.3\right) - b_{E_{m,g,corr}}}{a_{E_{m,g,corr}}} \tag{21}$$

$$S_{MOR} = \frac{f_{req,k} / k_v + t \cdot s_{\delta, f_{m,corr}} - b_{f_{m,corr}}}{a_{f_{m,corr}}} \tag{22}$$

$$S_{DEN} = \frac{\rho_{req,k} + t \cdot s_{\delta, \rho_{local,corr}} - b_{\rho_{local,corr}}}{a_{\rho_{local,corr}}} \tag{23}$$

where $E_{req,0,mean}$, $f_{req,k}$, and $\rho_{req,k}$ are the required characteristic values specified in EN 338 (European Committee for Standardization, 2016a), and S_{MOE}, S_{MOR}, and S_{DEN} are the corresponding IP thresholds.

For the multivariate models, the grading settings for bending MOE and bending strength were simplified to Eq. (24) and Eq. (25):

$$S_{MOE} = \frac{E_{req,0,mean} \cdot 0.95 + 2690}{10^3 \times 1.3} \tag{24}$$

$$S_{MOR} = f_{req,m,k} / k_v + t \cdot s_{\delta, f_{m,corr}} \tag{25}$$

Here, S_{MOE} and S_{MOR} represent the required $\widehat{E}_{m,g,corr}$ and $\widehat{f}_{m,corr}$, respectively. Together with the density setting derived from Eq. (23), the complete grading setting system can be established.

For both univariate and multivariate grading approaches, the final assigned grade was taken as the minimum grade among bending MOE, bending strength, and density, ensuring a conservative grading outcome in accordance with EN 14081–2 (European Committee for Standardization, 2018).

2.6. Statistical analysis

All statistical analyses related to regression modeling, grading setting derivation, and mechanical grading evaluation were performed using the R software environment (R Core Team, 2024). The extraction and calculation of knot-related indicators were conducted separately in a Python environment as described in **Section 2.3** (Python Software Foundation, 2025). Grading compliance was evaluated according to EN 14081–2 (European Committee for Standardization, 2018).

3. Results and discussion

3.1. Evaluation of model performance for knot detection and timber identification

Fig. 6 compares the detection performance of representative YOLO models for knot detection and timber identification. Overall, all evaluated models achieved high AP@50 values for knot detection (>0.90), indicating reliable identification of knots at a moderate Intersection over Union (IoU) threshold. Among them, YOLOv12n showed the best overall balance in knot detection performance, with the highest AP@50, F1-score, and AP@50:95 values, indicating superior overall accuracy and localization robustness.

For timber identification, all models performed consistently well, with AP@50 and F1 values close to 1.0. Although YOLOv12m achieved slightly higher localization accuracy under stricter IoU thresholds, the improvement over YOLOv12n was marginal. In contrast, YOLOv12n provided substantially higher computational efficiency while maintaining comparable overall performance.

Considering the overall balance between detection accuracy and computational efficiency, YOLOv12n was selected for subsequent analyses. The confidence and IoU thresholds were then optimized to 0.3 and 0.4, respectively, using a threshold search with increments of 0.1. During this process, F1-score was used as the primary criterion because it reflects the balance between precision and recall, while AP@50 and AP@50:95 were also considered to account for detection accuracy and localization robustness. For the subsequent calculation of knot-related indicators, the selected thresholds were intended to reduce missed knot detections while avoiding excessive false or duplicated detections that could affect KDR and CKDR calculation. The detection performance of the selected model under these settings is summarized in Table 4.

3.2. Prediction accuracy of maximum KDR and CKDR

Fig. 7 presents the regression relationships between the knot indicators predicted by YOLOv12n and their corresponding labeled values. For the maximum KDR (Fig. 7-**a**), both edge- and face-based predictions showed clear linear relationships with the labeled data. The coefficient of determination (R^2) was 0.57 for edge surfaces and 0.64 for face surfaces, indicating better prediction consistency on face surfaces. This difference is likely related to the more complete knot morphology and reduced occlusion on face surfaces compared with edge surfaces.

A similar pattern was observed for maximum CKDR (Fig. 7-**b**), with R^2 values of 0.61 and 0.64 for edge and face surfaces, respectively. Compared with maximum KDR, maximum CKDR showed a slightly higher overall agreement, suggesting that cumulative knot indicators are less sensitive to local detection uncertainties.

The highest agreement was obtained for the continuous grade-related indicator k_G, derived by linearly interpolating KDR and CKDR into grade intervals according to Eq. (3) to Eq**. (4)** (Fig. 7-**c**). The corresponding regression yielded an R^2 value of 0.69. This result indicates that the grading-oriented interpolation improves the consistency between predicted and labeled knot indicators.

Overall, the predicted knot indicators showed moderate but usable agreement with the labeled values. This level of agreement suggests that the predicted indicators retained part of the grading-relevant knot information and could therefore be used as supplementary variables in the subsequent correlation and regression analyses, although their prediction accuracy should not be overinterpreted.

3.3. Correlation analysis between knot indicators and mechanical properties

Fig. 8 shows the correlations between the knot-related indicators and the measured mechanical properties. Overall, the correlations with bending strength were consistently stronger than those with bending MOE, indicating that knot characteristics had a more direct influence on strength-related variability.

The predicted knot indicators showed correlation patterns comparable to those of the labeled values, and, in general, exhibited slightly stronger correlations than their labeled counterparts. Among all evaluated knot-related indicators, the strongest correlation with bending strength was obtained for the predicted continuous grade-related indicator $k_{G,p}$($r = -0.27$). For the individual knot descriptors, CKDR generally showed stronger correlations with bending strength than KDR. For example, the predicted maximum wide-face CKDR showed a stronger correlation with bending strength ($r = -0.25$) than the predicted maximum wide-face KDR ($r = -0.15$). These results indicate that the predicted knot indicators preserved the mechanical relevance of the labeled values and can therefore be used in the subsequent regression analyses.

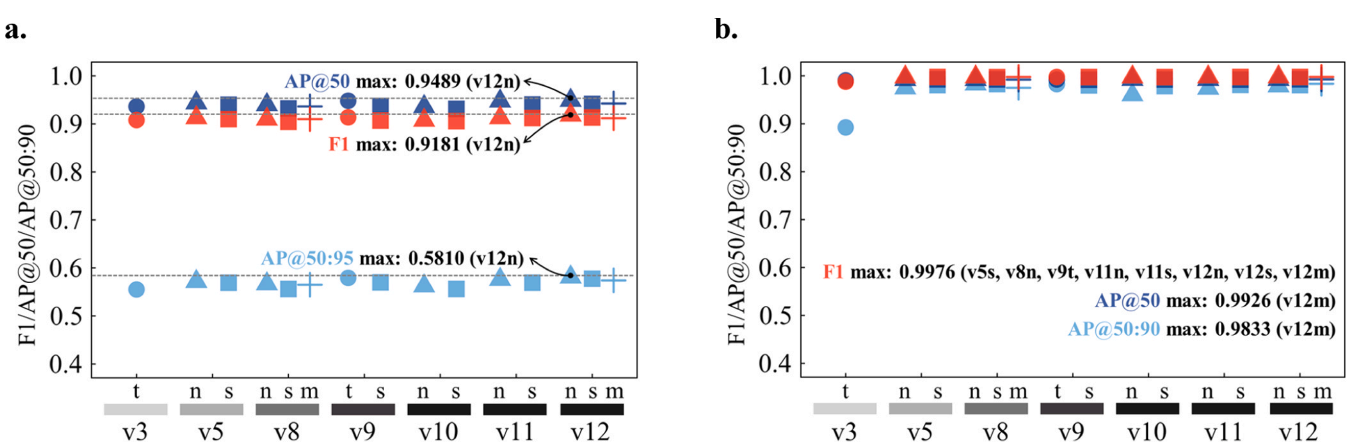

Fig. 6. Performance comparison of different YOLO models for (a) knot detection and (b) timber identification.

Table 4
Detection performance of the selected YOLOv12n model under the optimized confidence and IoU thresholds.

Model	Label	Precision	Recall	F1	mAP @50	mAP @50−95	Inference speed (ms)
YOLOv12n	All	0.9643	0.9532	0.9587	0.9675	0.7965	2.77
	Knot	0.9334	0.9063	0.9197	0.9426	0.6140	
	Timber	0.9953	1.0000	0.9976	0.9923	0.9790	

Note: mAP denotes the mean average precision averaged over all classes. When only a single class is considered, mAP is equivalent to AP.

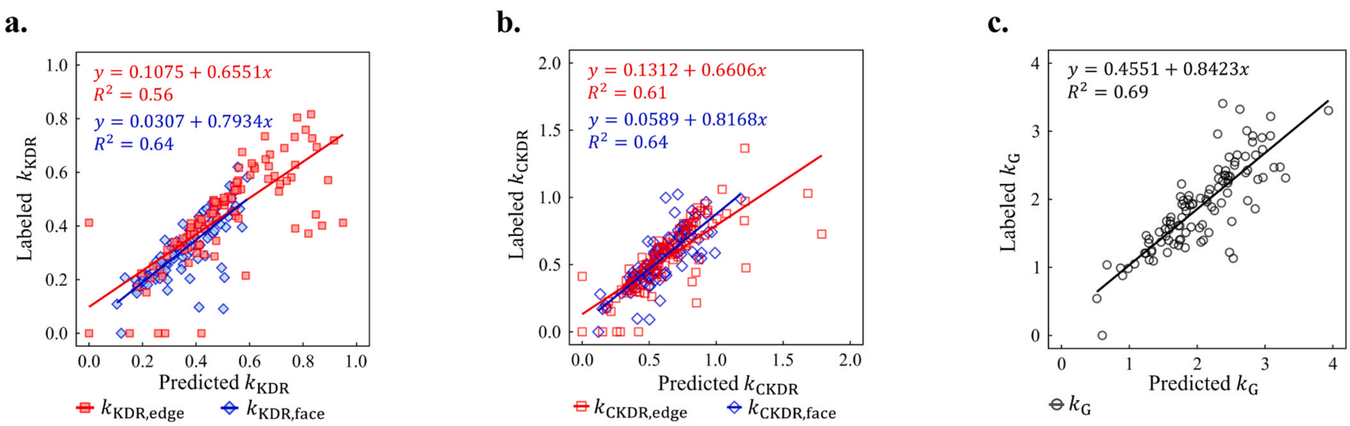

Fig. 7. Regression between YOLOv12n-predicted and labeled knot indicators: (a) maximum KDR, (b) maximum CKDR, and (c) continuous grade-related values from KDR and CKDR interpolation.

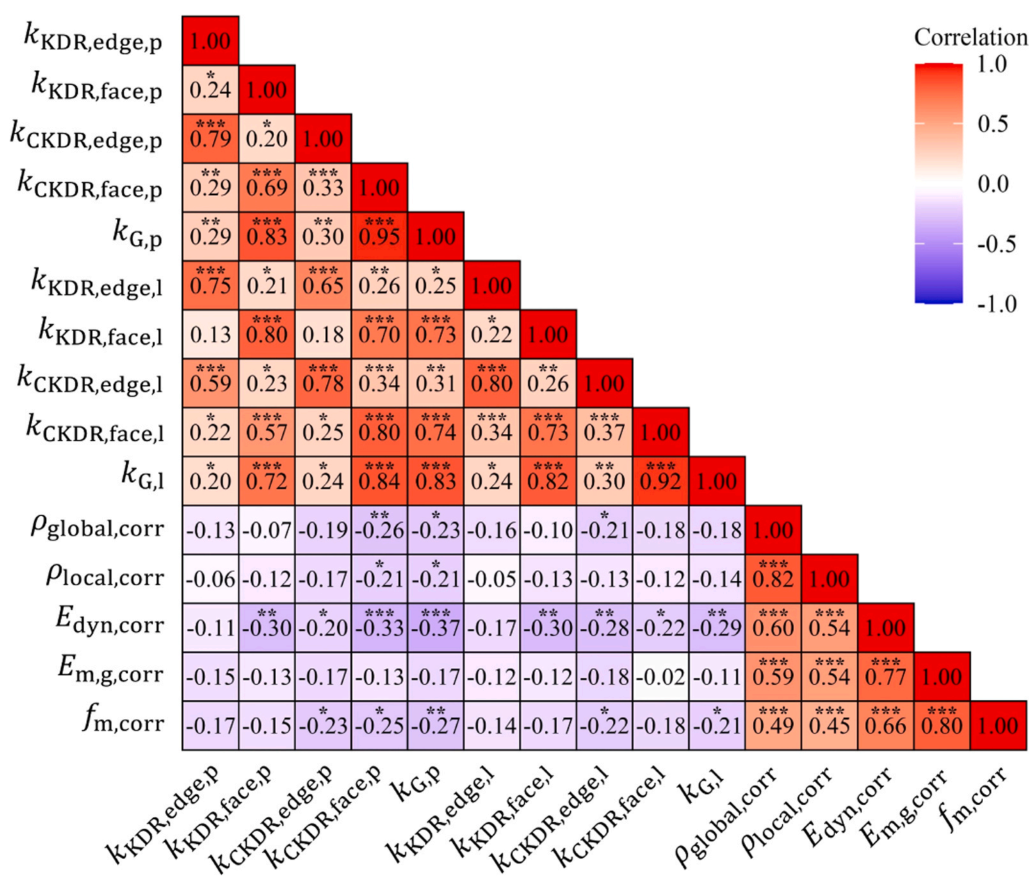

Fig. 8. Pearson correlation matrix showing the relationships among predicted and labeled knot indicators, density, dynamic MOE, and static bending properties. Note: Significance levels:. $p < 0.1$, * $p < 0.05$, ** $p < 0.01$, *** $p < 0.001$.

3.4. Regression models for mechanical grading

Before developing the regression models for grading, the basic physical and mechanical properties of the bending-test specimens were summarized (Table 5). The average moisture content was 14.58%, the mean global and local densities were 383 and 341 kg/m^3 , respectively, and the mean dynamic MOE, bending MOE, and bending strength were 8.8 GPa, 9.7 GPa, and 37.3 MPa, respectively. Among these properties, bending strength showed the greatest variability (CV = 25.85%).

For Chinese fir grading according to EN 338 (European Committee for Standardization, 2016a), univariate relationships were first examined between IPs and associated GDPs. The regression between local and global density yielded $R^2 = 0.67$ (Fig. 9-**a**). The corresponding lower prediction regression line was then used to determine global density IP values corresponding to the characteristic local density for each strength class. This lower prediction line was derived from the fitted regression line by subtracting $t \cdot s_{\delta,\rho_{\mathrm{local,corr}}}$, where $s_{\delta,\rho_{\mathrm{local,corr}}}$ is the standard error of the estimate for local density and $t = 1.645$ was used for the one-sided 5% lower prediction level under the large-sample assumption, as described in **Section 2.5.2**.

The regression between dynamic MOE and bending MOE yielded $R^2 = 0.60$ (Fig. 9-**b**). For bending strength, the corresponding univariate regression yielded $R^2 = 0.44$, and the same procedure was used to obtain the lower prediction line shown in Fig. 9-**c**. These results indicate that resonance frequency-based dynamic MOE provides a useful primary indicating property for predicting bending-related GDPs in Chinese fir, and its predictive ability is stronger for bending MOE than for bending strength.

Fig. 10 compares the R^2 values of multivariate regression models incorporating dynamic MOE together with either labeled or model-predicted knot indicators. The models were constructed both with and without interaction terms. Overall, the inclusion of knot indicators did not uniformly improve R^2 relative to the univariate regression model. In particular, narrow-face knot indicators provided little improvement, whereas wide-face indicators led to more consistent enhancement in the prediction of both bending MOE and bending strength.

For bending MOE, the model including the interaction term between dynamic MOE and the predicted maximum wide-face CKDR achieved the highest R^2 ($R^2 = 0.64$). A similar pattern was observed for bending strength, for which the corresponding model yielded the highest R^2 ($R^2 = 0.46$). Overall, the models using predicted knot indicators showed performance comparable to those using manually labeled indicators, with slightly higher R^2 values observed for some models. This may be related to the fact that the bounding-box-based prediction and maximum-window extraction procedure preserved the main grading-relevant knot information while reducing the influence of small local annotation differences. These results indicate that the predicted indicators were sufficiently reliable for use in regression-based grading analyses.

Table 5
Summary of the physical and mechanical properties of the timber samples (n = 102).

Sample statistics	Moisture content (%)	Density (kg/m^3)		Dynamic MOE (GPa)	Bending MOE (GPa)	Bending strength (MPa)
		Global	Local			
Mean	14.58	383	341	8.8	9.7	37.3
SD	1.82	52	39	1.6	1.5	9.7
CV	12.47	13.63	11.32	17.98	15.35	25.85
$P_{5,75}$	11.33	299	277	6.3	7.3	21.9
$P_{95,75}$	17.83	483	414	11.8	12.6	59.3

Note: Based on EN 14358 (European Committee for Standardization, 2016c), all statistical parameters except moisture content were assumed to follow lognormal distributions. $P_{5,75}$ and $P_{95,75}$ denote the 5th and 95th percentiles at 75% confidence. Moisture content showed no significant skewness and was assumed to follow a normal distribution.

It is also noteworthy that although the grade-related indicator $k_{\mathrm{G,p}}$ showed the strongest simple correlation with bending strength in Fig. 8, it did not yield the greatest improvement when incorporated into the multivariate regression models. This suggests that the indicator showing the strongest individual correlation is not necessarily the most effective variable in the multivariate grading framework, likely because multivariate model performance depends on the additional information contributed beyond that already represented by dynamic MOE.

In earlier studies, dynamic MOE alone often provided relatively high predictive performance for bending MOE, with reported R^2 values of about 0.56–0.81, whereas the addition of knot-related variables generally led to only limited further improvement, typically on the order of 0.01–0.04. For bending strength, the contribution of defect-related information was more variable. For example, when knot-related variables were added to models based solely on dynamic MOE, reported R^2 values increased from 0.15 to 0.20 and from 0.22 to 0.37 in one study (França et al., 2020), from 0.54 to 0.63 in another (Wright et al., 2019), and from 0.13 to 0.35 when other defect descriptors were also included (Barriola et al., 2021). These differences likely reflect variations in species, specimen geometry, defect characterization methods, and modelling approaches. Under the conditions examined in the present study, the results indicate that vision-based knot information can still provide supplementary predictive value beyond dynamic MOE for Chinese fir, although the improvement in predictive accuracy—particularly for bending strength—was somewhat lower than that reported before.

Fig. 11 further compares the predicted and measured values obtained from the univariate regression model and the multivariate regression model. Although the multivariate models improved the coefficients of determination, the scatter of data points around the 1:1 line changed only slightly. This suggests that the observed improvement mainly reflects better overall explanation of variance rather than a substantial tightening of individual predictions.

Overall, for Chinese fir, the regression results confirm that dynamic MOE remained the dominant predictor, while knot-related indicators provided additional but limited value. Among the evaluated variables, the predicted maximum wide-face CKDR showed the most effective supplementary contribution and was therefore used in the subsequent grading analyses.

3.5. Chinese fir grading results

Table 6 summarizes the regression models and associated statistical parameters used for grading, and Table 7 presents the corresponding IP settings derived for the relevant EN 338 (European Committee for Standardization, 2016a) strength classes according to the procedure described in **Section 2.5**. Based on these settings, preliminary size matrix was first obtained across the considered strength classes from C14 to C40 using the univariate regression model (Table 8). To comply with EN 14081–2 (European Committee for Standardization, 2018), which requires at least 20 specimens per grade for grading verification, grades with insufficient sample numbers were subsequently consolidated.

After consolidation, the final grade distribution consisted of C20, C14, and Reject (Table 9). The C14 class accounted for the largest proportion of the tested population (45.1%), followed by Reject (35.3%) and C20 (19.6%). Although the multivariate models incorporating knot-related indicators caused some redistribution of specimens among the preliminary strength classes, the consolidated grading outcome remained unchanged. These results indicate that resonance frequency-based dynamic MOE alone was able to provide a viable grading basis for the tested Chinese fir population.

Table 10 further shows that all three GDPs for both C14 and C20 satisfied the characteristic-value requirements specified in EN 338 (European Committee for Standardization, 2016a). The ratios of the derived characteristic values to the corresponding grade requirements followed the order: density < bending MOE < bending strength.

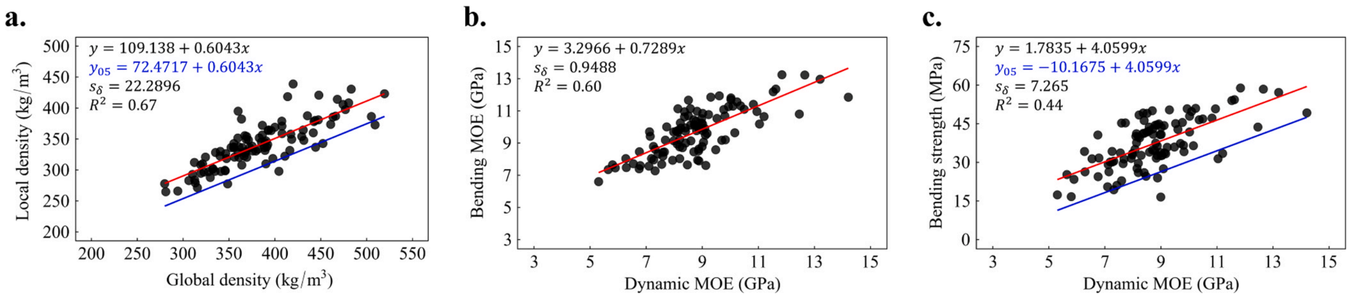

Fig. 9. Regression relationships for the density and bending-related properties used in grading: (a) local density versus global density, (b) bending MOE versus dynamic MOE, and (c) bending strength versus dynamic MOE.

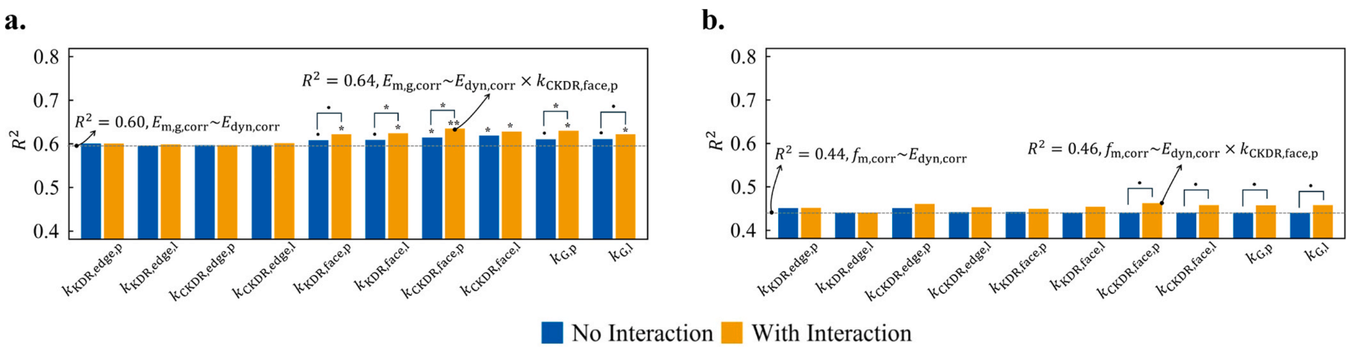

Fig. 10. Comparison of R^2 values for univariate regression using dynamic MOE and multivariate models incorporating dynamic MOE with knot indicators for predicting (a) bending MOE and (b) bending strength. Note: $E_{m,g,corr} \sim E_{dyn,corr}$ represents the univariate regression model $E_{m,g,corr} = b + a_1 \cdot E_{dyn,corr}$; similar notation applies to the univariate models for bending strength. The model $E_{m,g,corr} \sim E_{dyn,corr} \times k_{CKDR,face,p}$ denotes the multivariate regression $E_{m,g,corr} = b + a_1 \cdot E_{dyn,corr} + a_2 \cdot k_{CKDR,face,p} + a_3 \cdot E_{dyn,corr} \cdot k_{CKDR,face,p}$, with analogous notation for the multivariate bending strength models.

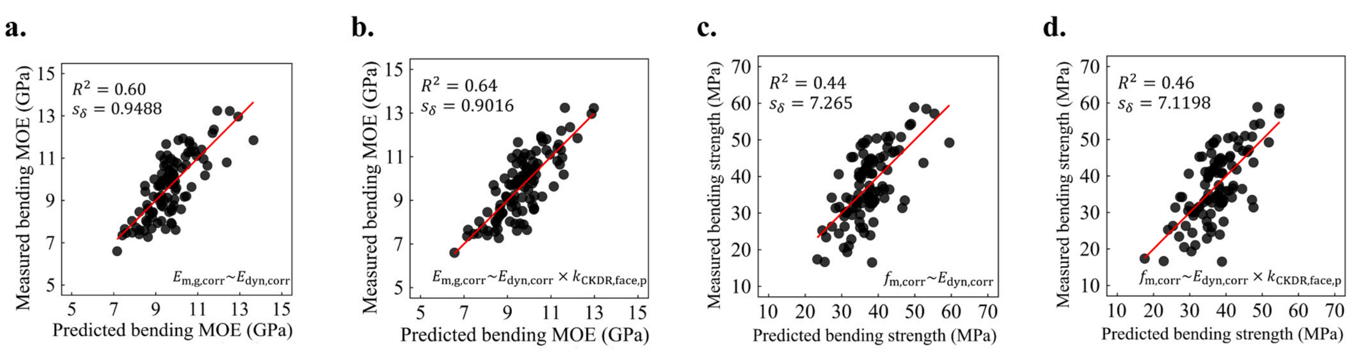

Fig. 11. Predicted versus measured bending MOE and bending strength obtained from the univariate and knot-based multivariate regression models: (a) univariate prediction of bending MOE, (b) multivariate prediction of bending MOE, (c) univariate prediction of bending strength, and (d) multivariate prediction of bending strength.

Table 6
Regression models for bending MOE and bending strength and statistical parameters required for grading setting calculations.

Model	R^2	a_1	a_2	a_3	b	s_δ	t	IP	GDP
$E_{m,g,corr} \sim E_{dyn,corr}$	0.60	0.7289			3.2966	0.9488	1.645	$E_{dyn,corr}$	$E_{0,mean}$
$f_{m,corr} \sim E_{dyn,corr}$	0.44	4.0599			1.7835	7.265		$E_{dyn,corr}$	f_k
$E_{m,g,corr} \sim E_{dyn,corr} \times k_{CKDR,face,p}$	0.64	0.4847	−4.0212	0.5961	4.7988	0.9016		$\widehat{E}_{m,g,corr}$	$E_{0,mean}$
$f_{m,corr} \sim E_{dyn,corr} \times k_{CKDR,face,p}$	0.46	2.0641	−35.3266	3.9851	19.9320	7.1198		$\widehat{f}_{m,corr}$	f_k
$\rho_{local,corr} \sim \rho_{global,corr}$	0.67	0.6403			109.138	22.2896		$\rho_{global,corr}$	ρ_k

Note: a_1, a_2, and a_3 are regression coefficients for the main dynamic MOE term, the knot-indicator term, and the interaction term, respectively; b is the intercept of the regression model; s_δ is the standard error of the estimate. The simplified notation t denotes the coefficient used to derive the lower prediction value, and $t = 1.645$ was adopted for the one-sided 5% lower prediction level under the large-sample assumption, as described in Section 2.5.2. Blank cells indicate that the corresponding term was not included in the model.

Table 7
Calculated settings of IPs for strength classes in EN 338 (European Committee for Standardization, 2016a).

Grade	Settings of IPs for univariate grading models			Settings of IPs including multivariate grading models		
	S_{MOE}	S_{MOR}	S_{DEN}	S_{MOE}	S_{MOR}	S_{DEN}
C30	10.347	9.102	508.899	10.838	38.617	508.899
C27	9.846	8.442	475.803	10.473	35.938	475.803
C24	9.344	7.782	459.255	10.108	33.260	459.255
C22	8.342	7.343	442.707	9.377	31.474	442.707
C20	7.841	6.903	426.159	9.012	29.688	426.159
C18	7.339	6.463	409.611	8.646	27.902	409.611
C16	6.337	6.023	393.063	7.915	26.117	393.063
C14	5.334	5.583	359.967	7.185	24.331	359.967

Note: In this study, the highest assigned grade of specimens reached only C30. Therefore, only the IP values for grade C30 and lower are presented. Settings of IPs for higher grades can also be calculated using the formulas described in Section 2.5 but are not listed here.

Table 11 also shows that density participated in determining the final grade of all rejected specimens, either individually or in combination with other GDPs. For the C14 and C20 classes, most specimens were governed either by density alone or by density together with bending MOE. Density alone or in combination with other GDPs determined the final grade of 91 out of 102 specimens (89.2%), whereas bending MOE participated in determining the final grade of 16 specimens (15.7%). These results indicated that grading under the EN 338 (European Committee for Standardization, 2016a) for the present material was controlled mainly by density, with bending MOE acting as a secondary controlling GDP.

Grading compliance was further evaluated according to EN 14081–2 (European Committee for Standardization, 2018) (Table 9). The global cost values corresponding to wrongly upgraded pieces did not exceed the required limit of 0.40, confirming that the grading settings satisfied the standard verification criteria. The final grading outcome is further illustrated on Fig. 12, which shows the relationships between the measured GDPs for the specimens assigned to the final grades.

Overall, these results confirm that resonance frequency-based dynamic MOE served as the primary indicating property for predicting the bending-related grade determining properties of fast-grown Chinese fir, while knot-related indicators provided supplementary information that only slightly affected the final grade distribution under the EN 338 (European Committee for Standardization, 2016a). Although the multivariate models improved the prediction of bending MOE and bending strength to some extent, their practical effect on grade yield remained limited, mainly because the final grading outcome was strongly constrained by density and the additional predictive contribution of the knot-related indicators was modest.

Although the multivariate models did not substantially improve overall grade yield under the EN 338 (European Committee for Standardization, 2016a), the density-dominated grading outcome

Table 8
Size matrix of strength class assignment based on the univariate regression grading model.

Optimum grade	Assigned grade											Total
	C40	C35	C30	C27	C24	C22	C20	C18	C16	C14	Reject	
C40	0	0	0	0	0	1	0	0	0	0	0	1
C35	0	0	0	0	0	0	0	0	0	0	0	0
C30	0	0	0	2	0	2	0	0	0	0	0	4
C27	0	0	1	1	1	1	1	0	1	1	0	7
C24	0	0	0	0	0	0	0	1	4	1	0	6
C22	0	0	0	0	1	2	3	1	1	6	1	15
C20	0	0	0	1	0	1	1	1	1	7	2	14
C18	0	0	0	0	0	0	0	1	0	7	6	14
C16	0	0	0	0	0	0	1	1	1	2	3	8
C14	0	0	0	0	0	0	0	2	1	5	13	21
Reject	0	0	0	0	0	0	0	0	0	1	11	12
Total	0	0	1	4	2	7	6	7	9	30	36	102

Note: Rows correspond to the target (optimum) strength classes, and columns correspond to the assigned strength classes. Diagonal elements indicate correctly graded pieces, the upper-right elements represent wrongly downgraded pieces, and the lower-left elements represent wrongly upgraded pieces.

Table 9
Verification of grading settings using the size matrix, elementary cost matrix, and global cost matrix.

Optimum grade	Assigned grade in the size matrix			Assigned grade in the elementary cost matrix			Assigned grade in the global cost matrix		
	C20	C14	Reject	C20	C14	Reject	C20	C14	Reject
C20	19	25	3	0	1.07	2.19	0	0.58	0.18
C14	1	20	22	1.43	0	1.01	0.07	0	0.62
Reject	0	1	11	3.02	1.11	0	0.15	0.02	0

Table 10
Derivation and verification of characteristic values for C14 and C20 strength classes in EN 338 (European Committee for Standardization, 2016a).

Grade	Strength class values specification in EN 338 (European Committee for Standardization, 2016a)			Derived characteristic values according to EN 384 (European Committee for Standardization, 2016b) and EN 14358 (European Committee for Standardization, 2016c)			Derived characteristic value / strength class value (%)			Number	Ratio (%)
	$f_{m,k}$ (MPa)	$E_{0,mean}$ (GPa)	ρ_k (kg/m^3)	$f_{m,k,d}$ (MPa)	$E_{0,mean,d}$ (GPa)	$\rho_{k,d}$ (kg/m^3)	$\frac{f_{m,k,d}}{f_{m,k}}$	$\frac{E_{0,mean,d}}{E_{0,mean}}$	$\frac{\rho_{k,d}}{\rho_k}$		
C20	20	9.5	330	32.430	11.637	330.065	162.2	122.5	100.0	20	19.6
C14	14	7	290	25.853	10.159	297.501	184.7	145.1	102.6	46	45.1
Reject				21.876	8.581	258.113				36	35.3
Total										102	100

Table 11
Numbers and proportions of specimens governed by different GDP combinations within each final assigned grade.

Assigned grade	Controlling GDP(s)					Total
	DEN	MOE	DEN + MOE	DEN + MOR	DEN + MOE + MOR	
C20	10 (50.0%)	6 (30.0%)	4 (20.0%)	0 (0.0%)	0 (0.0%)	20 (100%)
C14	42 (91.3%)	3 (6.5%)	1 (2.2%)	0 (0.0%)	0 (0.0%)	46 (100%)
Reject	33 (91.7%)	0 (0.0%)	0 (0.0%)	1 (2.8%)	2 (5.6%)	36 (100%)
Total	85 (83.3%)	9 (8.8%)	5 (4.9%)	1 (1.0%)	2 (2.0%)	102 (100%)

Note: DEN = density, MOE = bending MOE, and MOR = bending strength. The listed categories indicate the GDP(s) that individually or jointly determined the final assigned grade. Values are given as number of specimens, with percentages in parentheses.

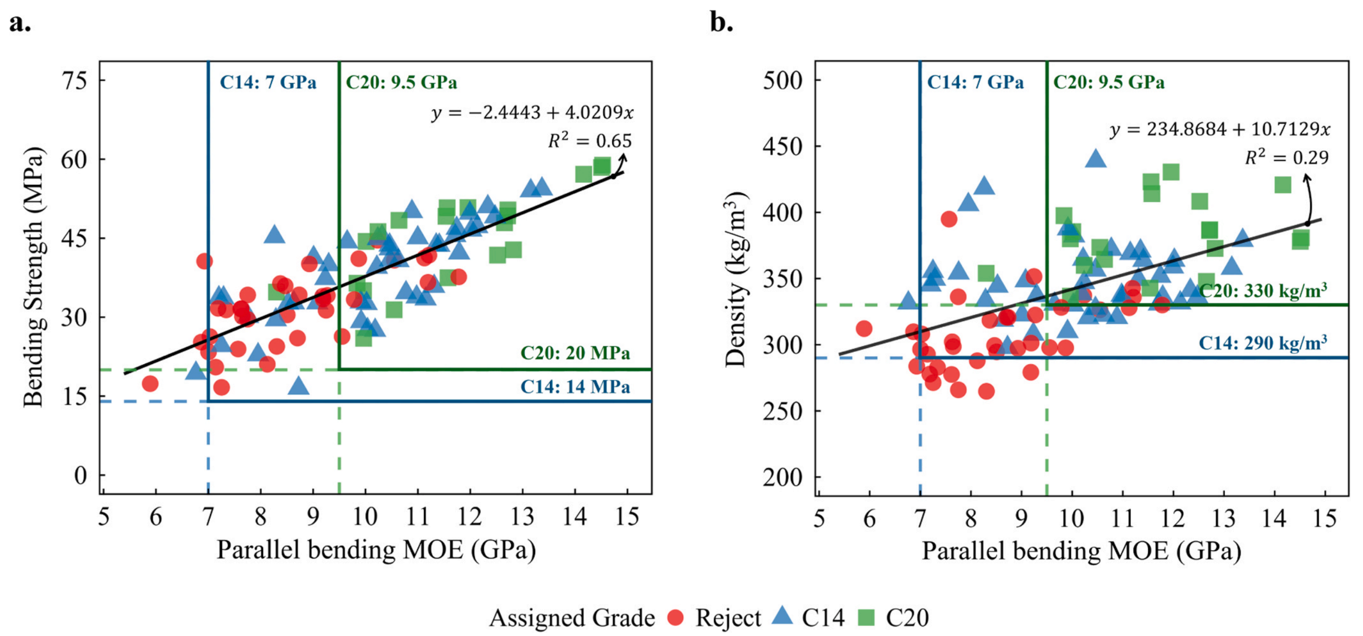

Fig. 12. Relationships between parallel bending MOE (E_0) and (a) bending strength ($f_{m,corr}$) and (b) density ($\rho_{local,corr}$) for the final grading results, including C14 and C20 thresholds in EN 338 (European Committee for Standardization, 2016a).

provides an important implication for the structural utilization of fast-grown Chinese fir. The results suggest that, under this framework, improving the final grade yield of this material is more strongly associated with satisfying the density requirement than with improving bending-property prediction alone. Therefore, material selection and resource allocation, such as screening boards with higher global density or considering differences related to growth region, provenance, and age class, may be more effective for increasing the proportion of material assigned to higher strength classes. In this context, automated knot quantification may provide useful support for defect assessment within existing visual grading workflows. Under certain conditions, it may also assist secondary selection within a grade, although this role is likely to remain subordinate to that of dynamic MOE.

Finally, the present findings should be interpreted within the scope of the investigated material. This study focused on fast-grown Chinese fir boards with a single nominal cross-section from a limited source range, and further work on broader material populations is needed to confirm the robustness of the derived grading relationships and thresholds. In addition, while the current knot-related indicators provided supplementary information beyond dynamic MOE, their practical contribution may depend on how defect descriptors are defined and extracted. Future studies should therefore examine broader datasets and refined knot characterization methods to further assess their value in resonance-based grading workflows.

4. Conclusion

This study evaluated whether resonance-based dynamic MOE, supplemented by vision-based knot indicators, could support the mechanical grading of fast-grown Chinese fir sawn timber under the EN 338 (European Committee for Standardization, 2016a) / EN 14081–2 (European Committee for Standardization, 2018) framework. The findings provide a preliminary but standard-linked assessment of the respective roles of dynamic MOE, density, and knot-related indicators within this grading framework. The main findings can be summarized as follows.

1. The selected YOLO-based detection workflow enabled automated quantification of knot-related indicators from surface images. The predicted knot indicators showed moderate agreement with manually derived reference values. The highest agreement between predicted and labeled knot-related indicators was obtained for the grade-related indicator (R^2 = 0.69). These results indicate that the predicted indicators retained part of the grading-relevant knot information and could be used as supplementary variables in the subsequent analyses.
2. Dynamic MOE alone showed good predictive ability for bending MOE ($R^2 = 0.60$) and bending strength ($R^2 = 0.44$). Incorporating the predicted maximum wide-face CKDR into multivariate models slightly improved the prediction of bending MOE (R^2 = 0.64) and bending strength ($R^2 = 0.46$). These results confirm that resonance-based dynamic MOE served as the primary indicating property, while

vision-based knot indicators provided measurable but limited supplementary value beyond dynamic MOE.

3. Density was identified as the governing grade determining property under the investigated material conditions. After consolidation according to EN 14081–2 (European Committee for Standardization, 2018), the final grade distribution was C20 (19.6%), C14 (45.1%), and Reject (35.3%). Most specimens were controlled by density, either alone or in combination with other GDPs, whereas the contribution of bending MOE was comparatively smaller. The multivariate models did not substantially improve grade yield compared with the univariate resonance-based model, indicating that the final strength-class assignment was mainly constrained by the density requirement rather than by the prediction of bending properties alone.
4. The grading settings derived from both univariate and multivariate models complied with EN 14081–2 (European Committee for Standardization, 2018), indicating that the proposed resonance-based grading workflow was statistically acceptable for the tested material population. However, the present results should be regarded as preliminary because the regression models and grading settings were derived from a relatively limited destructive dataset.

Overall, this study provides a preliminary validation of a standard-linked grading workflow integrating resonance-based dynamic MOE and vision-based knot indicators for fast-grown Chinese fir. The results confirm the effectiveness of dynamic MOE as a practical primary indicating property for grading fast-grown Chinese fir, clarify the supplementary but limited role of vision-derived knot indicators, and reveal that density is the main factor limiting higher strength-class assignment under the EN 338 (European Committee for Standardization, 2016a) framework.

Future work should examine Chinese fir from different provenances, age classes, and broader material populations, with particular attention to reducing the proportion of material that does not satisfy the density requirement, improving the achievable strength-class yield, and re-evaluating the grading value of other knot-related indicators under broader material conditions.

CRediT authorship contribution statement

Fanxu Kong: Writing – review & editing, Writing – original draft, Methodology, Data curation, Conceptualization. **Shuke Jia:** Investigation, Data curation. **Feibin Wang:** Writing – review & editing, Resources. **Tianjun Xie:** Investigation, Formal analysis. **Jinqiu Xie:** Investigation, Formal analysis. **Zeli Que:** Supervision, Project administration, Funding acquisition. **Jianzhang Li:** Resources, Project administration.

Declaration of Competing Interest

The authors declare that they have no known competing financial interests or personal relationships that could have appeared to influence the work reported in this paper.

Acknowledgments

The authors gratefully acknowledge the financial support provided by the National Key Research and Development Program of China (Grant No. 2024YFD2201204) and the Postgraduate Research & Practice Innovation Program of Jiangsu Province (Grant No. KYCX25–1415), and the China Scholarship Council.

Data availability

Data will be made available on request.

References

Abdeljaber, O., Habite, T., Olsson, A., 2023. Automatic estimation of annual ring profiles in Norway spruce timber boards using optical scanning and deep learning. Comput. Struct. 275, 106912. https://doi.org/10.1016/j.compstruc.2022.106912.
An, H., Liang, Z.H., Qin, M.M., Huang, Y.X., Xiong, F., Zeng, G.J., 2024. Wood defect detection based on the CWB-YOLOv8 algorithm. J. Wood Sci. 70, 26. https://doi.org/10.1186/s10086-024-02139-z.
Arriaga, F., Monton, J., Segues, E., Íñiguez-Gonzalez, G., 2014. Determination of the mechanical properties of radiata pine timber by means of longitudinal and transverse vibration methods. Holzforschung 68, 299–305. https://doi.org/10.1515/hf-2013-0087.
Barriola, M.J., Aira, J.R., Villanueva, J.L., 2021. Analytical models of the mechanical properties of Japanese larch (*Larix kaempferi* (Lamb.) Carr.) based on non-destructive testing and visual grading parameters. Wood Mater. Sci. Eng. 16, 94–101. https://doi.org/10.1080/17480272.2019.1626481.
British Standards Institution, 2007. BS 4978: Visual strength grading of softwood—Specification. BSI, London, UK.
Buslaev, A., Iglovikov, V.I., Khvedchenya, E., Parinov, A., Druzhinin, M., Kalinin, A.A., 2020. Albumentations: Fast and Flexible Image Augmentations. Information 11, 125. https://doi.org/10.3390/info11020125.
Collins, S., Fink, G., 2022. Modeling the tensile mechanical properties of silver birch timber boards. Constr. Build. Mater. 344, 128147. https://doi.org/10.1016/j.conbuildmat.2022.128147.
Ettelaei, A., Taoum, A., Nolan, G., 2022. Assessment of Different Measurement Methods/Techniques in Predicting Modulus of Elasticity of Plantation Eucalyptus nitens Timber for Structural Purposes. Forests 13, 607. https://doi.org/10.3390/f13040607.
European Committee for Standardization, 1997. EN 1309-1: Round and sawn timber. Method of measurement of dimensions - Sawn timber. CEN, Brussels, Belgium.
European Committee for Standardization, 2012. EN 408:2010+A1:2012: Timber structures - Structural timber and glued laminated lumber - Determination of some physical and mechanical properties.
European Committee for Standardization, 2016c. EN 14358: Timber structures - Calculation and verification of characteristic values. CEN, Brussels, Belgium.
European Committee for Standardization, 2016a. EN 338: Structural timber—Strength classes. CEN, Brussels, Belgium.
European Committee for Standardization, 2016b. EN 384: Structural timber—Determination of characteristic values of mechanical properties and density. CEN, Brussels, Belgium.
European Committee for Standardization, 2018. EN 14081-2: Timber structures - Strength graded structural timber with rectangular cross section - Part 2: Machine grading; additional requirements for type testing. CEN, Brussels, Belgium.
França, F.J.N., França, T.S.F.A., Seale, R.D., Shmulsky, R., 2020. Use of longitudinal vibration and visual characteristics to predict mechanical properties of No. S Southern pine 2×8 and 2x10 Lumber. Wood Fiber Sci. 52, 280–291. https://doi.org/10.22382/wfs-2020-026.
Gao, M.Y., Qi, D.W., Mu, H.B., Chen, J.F., 2021. A Transfer Residual Neural Network Based on ResNet-34 for Detection of Wood Knot Defects. Forests 12, 212. https://doi.org/10.3390/f12020212.
Gong, Y.C., Chen, X., Ren, H.Q., Liu, B.L., Zhang, H.M., Wang, Y.R., 2024. Theoretical and experimental studies on the bending properties of glued laminated timber manufactured with Chinese fir. Structures 68, 107149. https://doi.org/10.1016/j.istruc.2024.107149.
Huang, Q., He, L., Yin, T., Song, H., Wang, Z., Gong, M., 2023. Influences of lamination grade and loading waveform on fatigue performance and DOL effect of CLT fabricated from fast-growing Chinese fir. Constr. Build. Mater. 408, 133666. https://doi.org/10.1016/j.conbuildmat.2023.133666.
Jambreković, B., Veselčić, F., Ištok, I., Sinković, T., Živković, V., Sedlar, T., 2024. A Comparative Analysis of Oak Wood Defect Detection Using Two Deep Learning (DL)-Based Software. Appl. Syst. Innov. 7, 30. https://doi.org/10.3390/asi7020030.
Ji, M., Zhang, W., Han, J.K., Miao, H., Diao, X.L., Wang, G.F., 2024. A deep learning-based algorithm for online detection of small target defects in large-size sawn timber. Ind. Crops Prod. 222, 119671. https://doi.org/10.1016/j.indcrop.2024.119671.
Kılıç, Kenan, Kılıç, Kazım, Doğru, İ.A., Özcan, U., 2025. WD Detector: deep learning-based hybrid sensor design for wood defect detection. Eur. J. Wood Wood Prod. 83, 50. https://doi.org/10.1007/s00107-025-02211-5.
Kong, F.X., Lin, J.K., Ni, Y.H., Du, J.B., Jin, B.L., Jin, C.Y., Jia, S.K., Que, Z.L., Li, J.Z., 2025. A dynamic approach to grading fast-grown Chinese fir: Correlating resonance frequency-derived modulus with mechanical properties. Constr. Build. Mater. 505, 144798. https://doi.org/10.1016/j.conbuildmat.2025.144798.
Microsoft, 2021. VoTT: Visual object tagging tool. GitHub. 〈https://github.com/microsoft/VoTT〉.
Ministry of Agriculture, Forestry and Fisheries, 2019. JAS 1083: Sawn Lumber. MAFF, Tokyo, Japan.
Ministry of Agriculture, Forestry and Fisheries, 2023. JAS 1152: Glued laminated timber. MAFF, Tokyo, Japan.
Moriguchi, K., Shibata, N., Imai, M., Yamanouchi, M., Yoshida, T., 2016. Optimizing the Parameters of a Knot Assessment Model Based on the Visual Grading of JAS of Lumber. Mokuzai Gakkaishi 62, 133–145. https://doi.org/10.2488/jwrs.62.133.
National Forestry and Grassland Administration, 2018. LY/T 3039: Cross Laminated Timber. Standards Press of China, Beijing, China.
National Lumber Grades Authority, 2022. Standard grading rules for Canadian lumber. NLGA, Ottawa, ON, Canada.

Olsson, A., Oscarsson, J., 2017. Strength grading on the basis of high resolution laser scanning and dynamic excitation: a full scale investigation of performance. Eur. J. Wood Wood Prod. 75, 17–31. https://doi.org/10.1007/s00107-016-1102-6.
Oscarsson, J., Olsson, A., Enquist, B., 2014. Localized modulus of elasticity in timber and its significance for the accuracy of machine strength grading. Wood Fiber Sci. 46, 489–501.
Python Software Foundation, 2025. Python 3.9.23. 〈https://www.python.org/downloads/release/python-3923/〉.
R Core Team, 2024. R: A Language and Environment for Statistical Computing. R Foundation for Statistical Computing, Vienna, Austria.
Ridley-Ellis, D., Stapel, P., Baño, V., 2016. Strength grading of sawn timber in Europe: an explanation for engineers and researchers. Eur. J. Wood Wood Prod. 74, 291–306. https://doi.org/10.1007/s00107-016-1034-1.
Ridley-Ellis, D., Gil-Moreno, D., Harte, A.M., 2022. Strength grading of timber in the UK and Ireland in 2021. Int. Wood Prod. J. 13, 127–136. https://doi.org/10.1080/20426445.2022.2050549.
Schneider, C.A., Rasband, W.S., Eliceiri, K.W., 2012. NIH Image to ImageJ: 25 years of image analysis. Nat. Methods 9, 671–675. https://doi.org/10.1038/nmeth.2089.
Shi, A.Y., Bergsagel, D., Owen, J., Heisel, F., 2025. Scalable AI-driven automation for visual lumber grading. J. Clean. Prod. 533, 146986. https://doi.org/10.1016/j.jclepro.2025.146986.
Standardization Administration of China, 2018. GB/T 36407: Machine Stress Graded Lumber. Standards Press of China, Beijing, China.
Ultralytics, 2025. Ultralytics v8.3.152. GitHub. 〈https://github.com/ultralytics/ultralytics/releases/tag/v8.3.152〉.
Uzcategui, M.G.C., França, F.J.N., Seale, R.D., Senalik, C.A., Ross, R.J., 2023. Nondestructive Evaluation of 2 by 10 Southern Pine Lumber. For. Prod. J. 73, 186–193. https://doi.org/10.13073/FPJ-D-22-00054.
Wang, P.X., Liu, G.M., Li, F.R., Li, S.C., Milani, G., Abruzzese, D., 2025a. Assessment of knot-induced degradation in timber beams: probabilistic modeling and data-driven prediction of load capacity loss. Buildings 15, 2058. https://doi.org/10.3390/buildings15122058.
Wang, Y., Sun, X., Zhu, C., 2023. China's wood-based forest product imports and exports: trends and implications. Int. For. Rev. 25, 503–516. https://doi.org/10.1505/146554823838028184.
Wang, Z.C., Hao, J., Ren, H.Q., Gong, Y.C., 2025b. Roadmap for promotion and application of modern timber structures based on domestic forest resources (in Chinese). Constr. Sci. Technol. 61–67. https://doi.org/10.16116/j.cnki.jskj.2025.21.013.
Wright, S., Dahlen, J., Montes, C., Eberhardt, T.L., 2019. Quantifying knots by image analysis and modeling their effects on the mechanical properties of loblolly pine lumber. Eur. J. Wood Wood Prod. 77, 903–917. https://doi.org/10.1007/s00107-019-01441-8.
Yin, T.X., He, L., Huang, Q.Z., Gong, Y.C., Wang, Z.Q., Gong, M., 2024. Effect of lamination grade on bending and shear properties of CLT made from fast-growing Chinese fir. Ind. Crops Prod. 207, 117741. https://doi.org/10.1016/j.indcrop.2023.117741.